Check for updates

View Article Online
View Journal

Nanoscale
Advances

Accepted Manuscript

This article can be cited before page numbers have been issued, to do this please use: I. Stavarache, C. Palade, A. Slav, I. Dascalescu, A. Lepadatu, E. Matei, C. Besleaga, M. L. Ciurea, B. Kardynal and T. Stoica, *Nanoscale Adv.*, 2025, DOI: 10.1039/D5NA00138B.

This is an Accepted Manuscript, which has been through the Royal Society of Chemistry peer review process and has been accepted for publication.

Accepted Manuscripts are published online shortly after acceptance, before technical editing, formatting and proof reading. Using this free service, authors can make their results available to the community, in citable form, before we publish the edited article. We will replace this Accepted Manuscript with the edited and formatted Advance Article as soon as it is available.

You can find more information about Accepted Manuscripts in the Information for Authors.

Please note that technical editing may introduce minor changes to the text and/or graphics, which may alter content. The journal's standard Terms & Conditions and the Ethical guidelines still apply. In no event shall the Royal Society of Chemistry be held responsible for any errors or omissions in this Accepted Manuscript or any consequences arising from the use of any information it contains.

ROYAL SOCIETY OF CHEMISTRY

rsc.li/nanoscale-advances

View Article Online
DOI: 10.1039/D5NA00138B

Effect of molecule adsorption on conductivity of selectively grown interconnected 2D-MoS_2 atomically thin flakes structures

Ionel Stavarache,[1] Catalin Palade,[1] Adrian Slav,[1] Ioana Dascalescu,[1] Ana-Maria Lepadatu,[1]*

Elena Matei,[1] Cristina Besleaga,[1] Magdalena Lidia Ciurea[1,2], Beata E. Kardynal,[3,4] and*

*Toma Stoica[1]**

[1]National Institute of Materials Physics, 405A Atomistilor Street, 077125 Magurele, Romania

[2]Academy of Romanian Scientists, 54 Splaiul Independentei, 050094 Bucharest, Romania

[3]Peter Grünberg Institute 9 and JARA-FIT, Forschungszentrum Jülich, 52425 Jülich, Germany

[4]Department of Physics, RWTH Aachen University, 52074 Aachen, Germany

Open Access Article. Published on 24 February 2025. Downloaded on 2/24/2025 9:59:32 PM.
This article is licensed under a Creative Commons Attribution-NonCommercial 3.0 Unported Licence.

KEYWORDS: 2D-MoS_2, atomically thin layers, selective growth, molecule adsorption, field effect structures, spectral photocurrent

ABSTRACT:

Gas sensitivity of field-effect structures with 2D-MoS_2 channels selectively grown between Mo electrodes by Mo-CVD method has been investigated by measuring the effect of molecular adsorption from air on the device source-drain current (I_{sd}). The channels are composed of interconnected atomically thin MoS_2 grains, whose density and average thickness are varied by

Nanoscale Advances Accepted Manuscript

View Article Online
DOI: 10.1039/D5NA00138B

Open Access Article. Published on 24 February 2025. Downloaded on 2/24/2025 9:59:32 PM.
This article is licensed under a Creative Commons Attribution-NonCommercial 3.0 Unported Licence.

choosing two different distances (15 and 20 μm) between the Mo contacts. High response to the tested stimuli, i.e. molecule adsorption, illumination and gate voltage changes was shown. Huge, persistent photoconduction is induced by positive charge accumulation on traps most likely at grain boundaries and associated defects. I_{sd} increases at high vacuum, both in dark and under illumination. The relative dark current response to the change from air to high vacuum reaches up to 1000% at the turn-on voltage. Monitored during gradual change of air pressure, I_{sd} was a non-monotonic function, sharply peaking at about 10^{-2} mbar, suggesting molecule adsorption on different defect sites and orientations of adsorbed H_2O molecules capable of inducing the accumulation or depletion of electrons. Despite the screening of the disorder by extra electrons, #20μm sample remains more sensitive to air molecules on its surface. The high vacuum state was also investigated by annealing devices at temperatures up to 340 K in high vacuum followed by the measurement down to 100 K, revealing thermally stimulated currents and activation energies of trapping electronic states assigned to sulfur vacancies (230 meV) and other shallow levels (85–120 meV), possibly due to natural impurities, grain boundaries or disorder defects. The results demonstrate the high sensitivity of these devices to the molecule adsorption, making the technology promising for easy fabrication of chemical sensors.

1. INTRODUCTION

Strong interactions of nanometer thick layers of transitional metal dichalcogenides (2D-TMD) and other 2D materials with light and their good electronic transport lead to a large number

Nanoscale Advances Accepted Manuscript

View Article Online
DOI: 10.1039/D5NA00138B

Open Access Article. Published on 24 February 2025. Downloaded on 2/24/2025 9:59:32 PM.
This article is licensed under a Creative Commons Attribution-NonCommercial 3.0 Unported Licence.

Nanoscale Advances Accepted Manuscript

of reported potential applications.[1–4] In atomically thin 2D-MoS_2 layers, a strong increase of the exciton binding energy, dielectric confinement, spin-orbit coupling and large valence band spin-splitting, strongly influence the electronic properties making it attractive for photonics and spintronics.[5-8] The mono-layer (ML) of 2H-MoS_2 consists in an atomic Mo layer, cladded by two S layers. In a trigonal arrangement of atoms, the ML of 2H-MoS_2 is a semiconductor with a direct bandgap of about 1.9 eV. The 2D-MoS_2 with multilayers (MLs) remains a semiconductor, but the band gap becomes indirect and decreases with the number of ML layers, reaching the value of 1.2 eV in the bulk material. Through a different arrangement of the atomic layers, other phases are formed: 3R (rhombohedral) semiconducting; 1T (orthogonal) metallic.[9–11] The 2H-MoS_2 is the most thermodynamically stable phase.

The high surface-to-volume and high ON/OFF currents ratio in field-effect transistors (FET) make the 2D-MoS_2 FETs suitable for very sensitive optical, bio- and gas sensors.[12–14] Multicolor sensors and improved photovoltaic efficiency of solar cells can be obtained by alloying and formation of heterostructures of different 2D-TMD.[15–17] Due to the chemical and mechanical stability, ultrathin 2D-MOS_2 devices can be fabricated on different substrates, including flexible ones, for applications in electronics and optoelectronics as light emitters or detectors,[18–21] or various electrochemical applications such as batteries and supercapacitors, or catalytic electroreduction.[22–26] The modification of 2D materials by hetero-atoms or molecules through doping, intercalation or surface modification opens a wide perspective to tune the properties of 2D material for many applications such as magnetic, electrical, photoelectric, energy storage and conversion.[13, 27]

View Article Online
DOI: 10.1039/D5NA00138B

Open Access Article. Published on 24 February 2025. Downloaded on 2/24/2025 9:59:32 PM.
This article is licensed under a Creative Commons Attribution-NonCommercial 3.0 Unported Licence.

Different strategies for doping of 2D metal chalcogenides have been employed: (i) substitutional doping, (ii) charge transfer doping, (iii) intercalation doping and (iv) electrostatic field-effect doping.[28] Atoms, molecules, particles, support substrate or cladding layers can interact electrostatically with the 2D material and change its carrier concentration. They can change charge state of defects affecting electronic transport through films. Both effects can be influenced by light.[29] The exfoliated ML flakes of 2D-MoS_2 and 2D-WSe_2 have been reported to show a 50 and 3-fold increase in photoluminescence, respectively, after removing the adsorbed air molecules by annealing at 450 ^{o}C in vacuum. The photoluminescence increased by a factor of 100 in 2D-MoS_2 but decreased significantly in 2D-WSe_2 by exposure to pure H_2O and/or O_2 atmosphere.[30] Dipole-induced molecular doping has been shown to lead to accumulation or depletion of the electrons depending on the orientation of the molecular dipole in a collective molecular functionalization of monolayer MoS_2.[31] Through simulation, different adsorption sites preferred by these molecules are identified, for which the adsorption energy is negative, the more negative, the more stable the adsorption.[32–34] Defect sites and sites at or close to the edges are clearly preferable adsorption sites. The O_2 molecule preference site is on top of Mo from where it receives more electrons. For H_2O there are more favorable sites and molecule orientation with adsorption energy controlled by attractive interactions O–Mo and H-S, but also repulsive ones O-S and H-Mo.[31,32] Another possibility exists for H_2O molecules that of chemisorption by dissociating water into H and OH bound at different sites.[33] The H_2O and O_2 adsorption usually induce electron depletion in the MoS_2 layer, but in case of H_2O with its multiple adsorption sites and molecule orientations could also induce electron accumulation, at least as temporary unstable adsorption effect. Also, formation of

Nanoscale Advances Accepted Manuscript

View Article Online
DOI: 10.1039/D5NA00138B

Open Access Article. Published on 24 February 2025. Downloaded on 2/24/2025 9:59:32 PM.
This article is licensed under a Creative Commons Attribution-NonCommercial 3.0 Unported Licence.

Nanoscale Advances Accepted Manuscript

clusters of H_2O dipolar molecules adsorbed on 2D-MoS_2 surface could in principle work as collective dipole doping similar to that described in Ref. 31.

The electrostatic and/or chemical interaction of molecules adsorbed on atomically thin 2D-MoS_2 layers constitutes the working principle of highly sensitive FET detectors of inorganic or organic molecules.[13,14,35–39] However, the fabrication of 2D-MoS_2 FET sensors is generally based on isolated 2D flakes obtained either by exfoliation from bulk material or by CVD deposition with random nucleation on the support surface.[40] Fabrication of FET electrodes requires flake's localization and expensive, slow electron beam lithography technique and so cost-effective processes need to be developed to make the devices a viable technology beyond lab tests.

The device sensitivity to molecule adsorption is enhanced in FETs with high density of edge and boundary defect as preferential adsorption sites.[32–34] However, a high density of defects inside and at MoS_2 surface, as well as at the substrate interface, has an important charge trapping effect that strongly affects the field effect characteristics, inducing large hysteresis through electronic and molecular trapping-detrapping phenomena, resulting in a low level of source-drain dark current and reduced mobility. In addition to the quality of the 2D-MoS_2 material, the performances of FETs depend on the device fabrication method and the used measurement conditions (contact resistance, free surface passivation, measurement atmosphere, history of external stimuli, etc.). It is generally accepted so far that 2D-MoS_2 with the best crystalline quality was obtained in exfoliated flakes from the bulk. Even so, the electron mobility values reported in literature for measurements on single exfoliated flake 2D-MoS_2 FETs vary over a wide range of 0.1 – 200 cm^2/Vs.[41,42] The balance between intrinsic doping and the density of trapping centers

View Article Online
DOI: 10.1039/D5NA00138B

Open Access Article. Published on 24 February 2025. Downloaded on 2/24/2025 9:59:32 PM.
This article is licensed under a Creative Commons Attribution-NonCommercial 3.0 Unported Licence.

depends on the 2D-MoS_2 fabrication method and its optimization. By introducing structural defects through optimal incorporation of 1T metallic domains into exfoliated 2H-MoS_2 flakes by a mild oxygen plasma treatment to increase the layer conductivity, a high field-effect mobility of 237 cm^2/Vs was achieved compared to 7 – 43 cm^2/Vs in pristine flakes.[43] In contrast, due to trapping defects induced by exposure to oxygen above 2 mbar pressure, the hysteresis of the transfer characteristics of the exfoliated multilayer FETs was strongly increased, while the mobility was significantly reduced from 52 to 15 cm^2/Vs.[44] Hysteresis in the transfer characteristics of 2D-MoS_2low mobility FETs (0.3 – 6 cm^2/Vs) and its correlation with the charge trapping and the exposure to H_2O and O_2 effects, as well as the energy position of the trapping levels in the gap have also been intensively investigated in a series of publications.[45–47] By gold-assisted mechanical exfoliation, ultra-large monolayers (on centimeter scale) were obtained on Al_2O_3/Si substrate exhibiting a compressive strain of -0.25%, n-doping of $\approx 5 \times 10^{12}$ cm^{-2} and mobility of 2.3 cm^2/Vs.[48] Films of interconnected (edge-to-edge contact) MoS_2 exfoliated nanoflakes were produced on large area by self-assembled tiling at the planar interface between two immiscible liquids, exhibiting a FET mobility of 0.73 cm^2/Vs.[49] MoS_2 exfoliated nanosheets FETs have been measured with four-terminal electrical device to eliminate any contact contributions and reported in Ref. 50 showing that there are two classes of FETs mobility with distinct behavior: the mobility decreases (increases) with temperature due to dominant phonon scattering (due to impurity scattering and high contact resistance) at devices with room temperature (RT) mobility higher (lower) than 30 cm^2/Vs. To avoid direct contact of MoS_2 with the photoresist and the ambient environment during the FET fabrication process, a SiO_2 protective layer was used that was selectively etched on the

Nanoscale Advances Accepted Manuscript

View Article Online
DOI: 10.1039/D5NA00138B

Open Access Article. Published on 24 February 2025. Downloaded on 2/24/2025 9:59:32 PM.
This article is licensed under a Creative Commons Attribution-NonCommercial 3.0 Unported Licence.

contact areas to improve the FET contacts, thus achieving a mobility of 42 cm^2/Vs, ~20 times increased compared to a MoS_2 FET fabricated without the SiO_2 protective layer.[51] Intentionally aged 2D-MoS_2 FETs have shown a significant decrease of the electron mobility to 0.5 cm^2/Vs compared to as-fabricated devices of up to 8 cm^2/Vs, but better stability of the device working as selective gas sensor by detecting the current variation and low-frequency noise induced by exposure to air and vapors of polar and non-polar solvents.[52] The trapped charges and related hysteresis giving rise to the unscreened Coulomb scattering and/or the variable range hopping in MoS_2 FET have been also studied in Ref. 47. CVD grown 2D-MoS_2 using sulfur gas phase as precursor showed an average FET mobility value of 0.12 cm^2/Vs for sulfurization of very thin Mo metal films, while in the case of Mo oxide film a very low mobility of 10^{-4} cm^2/Vs was reported.[53,54,41]

The selective growth of 2D-MoS_2 at predefined positions on the surface of supports is one of the promising solutions for a mass production of 2D-MoS_2 FET devices. The nucleation and selective CVD growth of MoS_2/WSe_2 on c-Al_2O_3 or a-HfO_2 have been demonstrated using vapor precursors of sulfur and oxides of Mo and W and a sacrificial SiO_2 mask with several microns wide windows.[55] Selective growth of 2D-MoS_2 has also been achieved on structured Mo supports by CVD deposition with sulfur vapor and Mo oxide as precursors, the oxide either from MoO_3 powder or from oxidation of Mo pads by oxygen from the vacuum leaks.[56,57] In principle, selective growth at the desired sites can be also achieved by sulfurization of MoO_x thin films pre-deposited through a photolithographic mask, but the process still requires further optimization to reduce the MO_2 doping at high temperatures and improve film uniformity while maintaining a low oxide

Nanoscale Advances Accepted Manuscript

View Article Online
DOI: 10.1039/D5NA00138B

Open Access Article. Published on 24 February 2025. Downloaded on 2/24/2025 9:59:32 PM.
This article is licensed under a Creative Commons Attribution-NonCommercial 3.0 Unported Licence.

sublimation rate.[58–61] The selective nucleation and growth of 2D-MoS_2 around the oxide windows on structured SiO_2/Si supports was achieved by the vapor transport deposition directly from MoS_2 powder.[62] The films consisting of multi-crystalline flakes with the range of sizes and density nucleated and grew around the substrate patterns. A better control of the selective nucleation of 2D-MoS_2 at the proximity of Mo electrodes was obtained by simultaneous diffusion of Mo native oxide from the Mo electrodes and its reaction with sulfur vapors (Mo-CVD method).[63] An additional advantage of this growth method is its bottom-up approach to making devices: source-drain Mo-electrodes are pre-deposited and MoS_2 film is self-aligned and in intimate contact with them, without post-growth photolithographic process, avoiding the surface contamination with resists after common photo- or electron-beam device fabrication, very important for gas sensor fabrication.[64–66] Photo-FET devices prepared using this method showed a responsivity of 25 A/W and more than 4 orders of magnitude variation of the photo-to-dark current ratio, which is adjustable by changing the gate voltage. The field-effect structures fabricated by this simple method could be used for various applications, such as, for example, the detection of the adsorbed molecule, but to our knowledge, there are no reports of such studies.

In this work, we investigate the response to adsorbed air molecules on selectively grown 2D-MoS_2 interconnected flakes obtained by Mo-CVD method with pre-deposited Mo electrodes. The FETs were fabricated in the simplest way, by directly bonding the contacts after the growth of 2D-MoS_2, avoiding surface contamination with photoresist traces through any additional photolithographic metallization process. The selectively grown 2D-MoS_2 layers cover the gap between Mo source-drain contacts of field effect structures, ensuring not only the selective growth

Nanoscale Advances Accepted Manuscript

View Article Online
DOI: 10.1039/D5NA00138B

Open Access Article. Published on 24 February 2025. Downloaded on 2/24/2025 9:59:32 PM.
This article is licensed under a Creative Commons Attribution-NonCommercial 3.0 Unported Licence.

Nanoscale Advances Accepted Manuscript

in the active areas, but also intimate contacts with pre-deposited Mo electrodes. We study devices with electrodes spaced at 15 µm and 20 µm, which we refer to as #15µm and #20µm, respectively, and which we expect to have different densities and average thickness of the MoS_2 flakes since they were grown at the same growth parameters. Desorption of molecules from air (O_2 and H_2O) by exposure to high vacuum (HV) results in the increase of both dark and photo- currents compared with those measured at atmospheric pressure. Both #15µm and #20µm samples exhibit similar behavior when measured during vacuum annealing at 340 K and subsequent measurements of the current-temperature dependence at low temperatures down to 100 K. We propose that depending on orientation of the adsorbed H_2O molecules from air and on adsorption sites on the 2D-MoS_2 layer one can observe accumulation (at least as temporary effect) or depletion of electrons in MoS_2.

2. EXPERIMENTAL METHODS

Sample fabrication. To prepare the growth substrate, a Mo layer of 30 nm thickness was deposited by magnetron sputtering of SiO_2(300nm)/c-Si and patterned by photolithographic liftoff process to form multi-finger contacts to be used in FETs as source-drain contacts, as illustrated in Fig. 1a by the bottom bird's eye view image. Each contact consists of a large square pad of 500 µm side and a number of fingers that fit along the lateral length of the pad. The Mo fingers were spaced at 15 µm or 20 µm, defining the channel length L of the FET device. The overlap of the opposing source and drain fingers is designed to be W_i = 40 µm corresponding to an active area of selectively grown 2D-MoS_2 of L$\times$$W_i$ for each overlapping region of the opposing fingers (see a detailed image of the selective growth in Fig. 1b). The total channel width of the FET is the sum of all finger

View Article Online
DOI: 10.1039/D5NA00138B

Open Access Article. Published on 24 February 2025. Downloaded on 2/24/2025 9:59:32 PM.
This article is licensed under a Creative Commons Attribution-NonCommercial 3.0 Unported Licence.

overlap regions W = $\Sigma_i W_i$ which corresponds to a total active area measured in squares of side L (W/L) of 48 and 28 for the #15μm and #20μm samples, respectively. Selective growth of atomically thin MoS_2 with Mo supplied from the deposited layer was obtained by Mo-CVD method in a 3-zone horizontal quartz tube furnace (Carbolite HZS). The growth substrate was placed at higher temperatures (750 °C) zones of the furnace while the crucible with sulfur powder was placed in the low temperature, 200 °C, zone. The selective growth took place over 30 min by simultaneous surface diffusion of native MoO_2 from the Mo surface and its chemical reaction with S vapor transported by 20 sccm Ar flux at 100 mbar pressure. Once the growth was finished, the FET device was completed by making a GaIn ohmic contact on the backside of the Si substrate that was used as the gate electrode. More details can be found in Ref. 63.

Morphology, structure and photosensitivity characterization methods. The morphology of the selectively grown films was investigated by optical and scanning electron microscopy (SEM) (Zeiss Gemini 500). The information about the nature of the crystalline structure and the layer thicknesses was obtained from Raman spectroscopy, using a LabRAM HR (Horiba Jobin-Yvon) with 532 nm excitation. The source-drain current, I_{sd}, as a function of source-drain, V_{sd}, and gate, V_g, voltages was monitored under monochromatic light with the wavelength above the absorption edge. Transimpedance characteristics (I_{sd} as a function of V_g for set V_{sd}) were recorded using a Keithley 236 Source Measure Unit and a Keysight B2902A Source Measure Unit. A Newport Cornerstone™ 260 monochromator was used for sample illumination. All measurements presented in this paper have been performed in a cryostat, in air and/or vacuum, at room temperature without any

Nanoscale Advances Accepted Manuscript

View Article Online
DOI: 10.1039/D5NA00138B

Open Access Article. Published on 24 February 2025. Downloaded on 2/24/2025 9:59:32 PM.
This article is licensed under a Creative Commons Attribution-NonCommercial 3.0 Unported Licence.

prior annealing, except for those in the last subchapter 3.4 regarding the temperature dependence of the current in the range 100–240 K, when the samples were first treated in high vacuum up to 340 K.

3. RESULTS AND DISCUSSION

The schematic diagram of the used field-effect device with source-drain finger contacts is shown in Fig. 1a. Under ambient pressure, air molecules are adsorbed on the MoS_2 surface modifying its conductivity via trapping of charges or electrostatic charging of the layers. O_2 and H_2O molecules are the most often considered adsorbates. As shown in Introduction, H_2O and O_2 adsorption usually induces electron depletion in the MoS_2 layer, but in case of H_2O molecule with its multiple adsorption sites and orientations electron accumulation could also be induced (sketch in Fig. 1a).

2D-MoS_2 was selectively grown around Mo patterns by the Mo-CVD method described in Ref. 63. By this method, the MoS_2 layers with intimate contact to the Mo patterns are obtained through simultaneous processes of diffusion and sulfurization of the oxide previously formed on the Mo surface. A detail of Mo finger contacts patterns is exemplified by the optical image in Fig. 1b (MoS_2 layer (green contrast) surrounds the Mo contacts (yellow)). We succeeded to selectively grow MoS_2 up to 10 – 15 µm distance from Mo pads, enough to cover by 2D-MoS_2 the space between source-drain Mo finger contacts, as marked in Fig. 1b, up to a gap of 20 µm. Such structure grown on conductive Si substrate covered by 300 nm SiO_2 isolation layer can be used as field effect transistor with Mo source-drain contacts and Si substrate as back gate.

Nanoscale Advances Accepted Manuscript

View Article Online
DOI: 10.1039/D5NA00138B

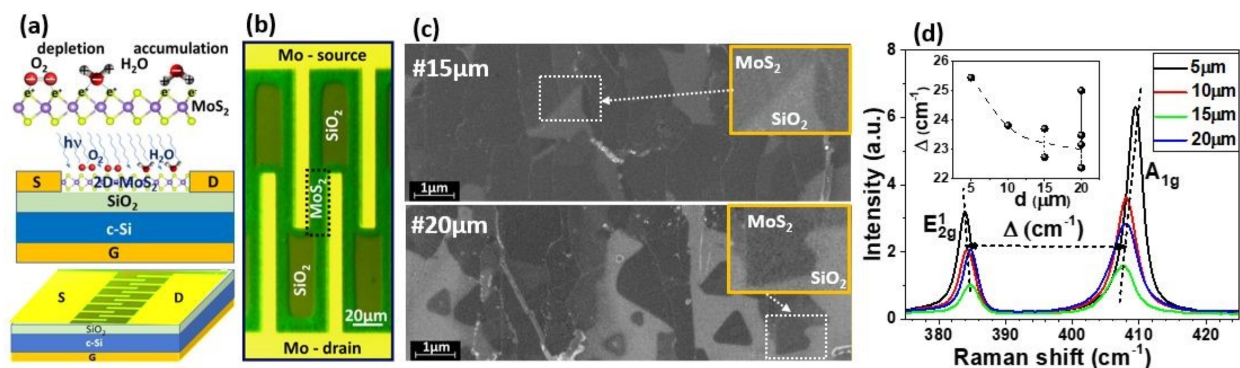

Fig. 1 (a) Schematic diagram of the electron depletion and accumulation in 2D-MoS_2 by adsorption of O_2 and H_2O molecules from air, the cross-section and bird view of the device with selectively grown MoS_2 between Mo finger contacts; (b) optical image detail of selectively grown 2D-MoS_2 around Mo finger contact patterns; (c) comparison of high resolution SEM images of 2D-MoS_2 acquired from gap between Mo electrodes placed top and down relative to the SEM images of #15μm and #20μm samples (dark areas – MoS_2 MLs; lighter areas – SiO_2); (d) representative Raman spectra of 2D-MoS_2 for different gap lengths (inset shows dependence Δ between A_{1g} and E_{2g}^1 peaks as a function of gap length).

The selectively grown 2D-MoS_2 layer consists of interconnected flakes of different thicknesses, from single ML to a stack of few ML.[63] The interconnected MoS_2 flakes form conductive layers between Mo source-drain finger contacts dominated by many grain boundaries and flake edge defects. The density of the flakes and the average thickness decrease with the distance (gap) between Mo fingers. Fig. 1c shows a comparison between high resolution SEM images acquired from the 2D-MoS_2 layer grown between source-drain Mo fingers distanced by 15 μm and 20 μm, from samples #15μm and #20μm, respectively. As can be seen, the isolated MoS_2 flakes more frequently appear in #20μm sample than #15μm. Moreover, distinct conductive channels of interconnected flakes between Mo electrodes are formed in #20μm sample, some of them being interrupted. The fluctuation in flake density is also associated with the fluctuation in average thickness found by local μ-Raman measurements for different positions of the laser spot. Representative Raman spectra within the frequency range of the specific A_{1g} and E_{2g}^1 peaks of

Open Access Article. Published on 24 February 2025. Downloaded on 2/24/2025 9:59:32 PM.
This article is licensed under a Creative Commons Attribution-NonCommercial 3.0 Unported Licence.

Nanoscale Advances Accepted Manuscript

View Article Online
DOI: 10.1039/D5NA00138B

Open Access Article. Published on 24 February 2025. Downloaded on 2/24/2025 9:59:32 PM.
This article is licensed under a Creative Commons Attribution-NonCommercial 3.0 Unported Licence.

MoS_2 acquired from devices with different size of the gap between Mo fingers are shown in Fig. 1d. The frequency difference Δ between these peaks can be used to evaluate the mean thickness in number of MLs, based on the calibration given in Ref. 49. As revealed by the inset of the Fig. 1d, the mean thickness decreases by increasing the gap between electrodes from 5 µm to 15 µm, Δ value decreasing from 25.5 cm^{-1} (~6 MLs) to 23.0 cm^{-1} (~3 MLs). Thickness fluctuation ranges of 2.7 – 3.6 and 2.4 – ~6.0 MLs have been clearly detected in #15µm and #20µm, respectively, as results from data of Fig. 1d inset. These large thickness fluctuations indicate that thin intercalated flakes of 1–2 MLs thickness have large probability to be components of channels, thus controlling their conductance. Additionally, the larger number of interconnected flakes, with corresponding grain boundaries and edge defects makes #15µm and #20µm devices promising for sensing adsorbed molecules.

3.1 Molecule adsorption effects on gate voltage dependence

The gate voltage dependences of I_{sd} (V_{sd} =1.0 V) in #15µm and #20µm samples in dark and under illumination with monochromatic light, in vacuum of different pressures and in air (at atmospheric pressure) collected in Fig. 2, show similar behavior: increased dark current and current during light exposure in vacuum in comparison with I_{sd} currents measured in air. For better comparison between samples, the current in Fig. 2a,b is normalized to the total area of the 2D-MoS_2 active layer between finger contacts measured in squares of L^2 area (L is the channel length of 15 µm and 20 µm, the samples #15µm and #20µm have 48 □ and 28 □ squares, respectively).

Nanoscale Advances Accepted Manuscript

View Article Online
DOI: 10.1039/D5NA00138B

Open Access Article. Published on 24 February 2025. Downloaded on 2/24/2025 9:59:32 PM.
This article is licensed under a Creative Commons Attribution-NonCommercial 3.0 Unported Licence.

Nanoscale Advances Accepted Manuscript

The normalized I_{sd}(pA/□) represents the product $\sigma_{sd} V_{sd}$ of the surface conductivity σ_{sd} and source-drain voltage V_{sd}.

At V_g = 0 V, in dark, sample #15μm is depleted at atmospheric pressure and weakly n-doped in vacuum (Fig. 2a). Removal of adsorbed molecules from the surface freed electrons available for electronic transport and the current reaches about 1.0 pA/□. Sample #20μm is depleted in dark at all pressures at V_g = 0 V and much larger positive voltages are needed to accumulate free electrons (Fig. 2b). 4.4 times lower current density at the same voltages (2.0 V) above the turn on voltage flows through the #20μm device than the #15μm (e.g. 1.75 pA/□ at V_g = 2 V for #15μm device and 0.40 pA/□ at V_g = 5 V for #20μm device, both in dark and in air). It means that #20μm device has more electron traps. As shown in Fig. 1c, the lower density of interconnected MoS_2 flakes, forming separated conductive channels, some of them being interrupted in #20μm may also explain the lower surface conductance.

View Article Online
DOI: 10.1039/D5NA00138B

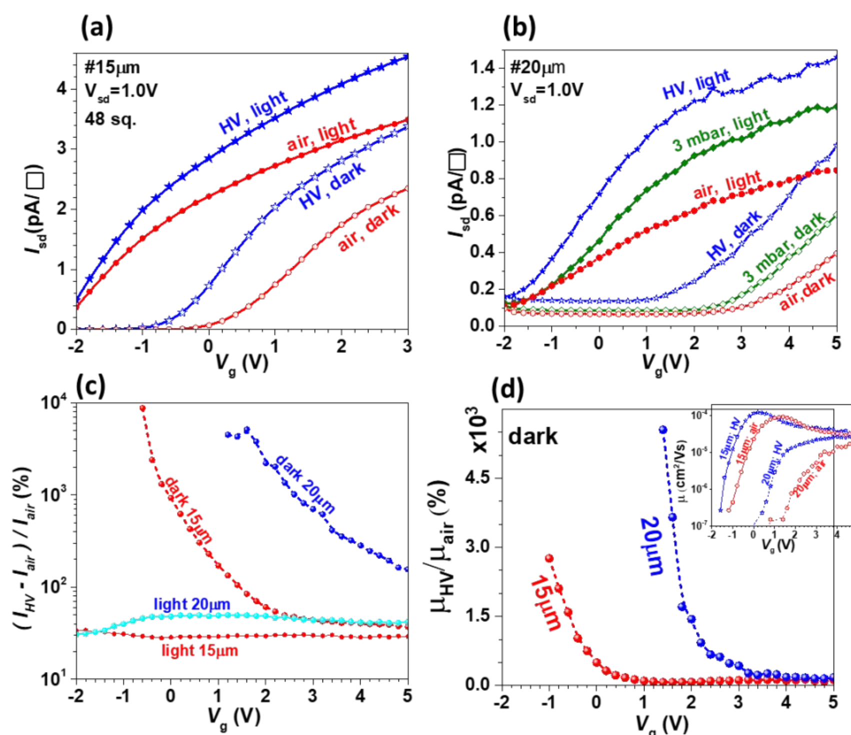

Fig. 2 Gate-voltage dependence of dark source-drain current and photocurrent under monochromatic light measured on samples at room temperature: (a) #15μm (light of λ=600 nm) and (b) #20μm (light of λ=570 nm) samples in vacuum, in air at atmospheric and reduced pressures (the current is normalized to the number of L^2 squares (sq.) of the active MoS_2 area, L being the respective channel length); (c) Relative differences between currents measured at high vacuum (HV) of 2 x 10^{-5} mbar (I_{HV}) and in air (I_{air}) of atmospheric pressure on samples #15μm and #20μm (relative differences $(I_{HV}-I_{air})/I_{air}$ for dark current and photocurrent under illumination with monochromatic light are shown); (d) gate voltage dependence of the mobility obtained from the dark transfer curves in figures (a) and (b) measured in air and at HV.

Illumination introduces larger density of free electrons as can be seen from the shift of the turn on voltage of both devices. #15μm sample is already turned on at -2V, #20μm sample turns-on at around -2V. The shift of the turn-on voltage is larger for the latter device, which could indicate that the photogenerated carriers reduce the potential disorder freeing the trapped electrons more than in #15μm sample. Despite the screening of the disorder by extra electrons, #20μm sample remains more sensitive to air molecules on its surface. This is better revealed by the changes of the source-drain currents due to molecular desorption at HV of 2 x 10^{-5} mbar relative

Open Access Article. Published on 24 February 2025. Downloaded on 2/24/2025 9:59:32 PM.
This article is licensed under a Creative Commons Attribution-NonCommercial 3.0 Unported Licence.

Nanoscale Advances Accepted Manuscript

View Article Online
DOI: 10.1039/D5NA00138B

Open Access Article. Published on 24 February 2025. Downloaded on 2/24/2025 9:59:32 PM.
This article is licensed under a Creative Commons Attribution-NonCommercial 3.0 Unported Licence.

to the values measured in air, as depicted by gate voltage dependence of $(I_{HV}-I_{air})/I_{air}$ in Fig. 2c for both samples #15μm and #20μm. The relative response of the illuminated samples to the change of pressure is weak and also very weakly dependent on the gate voltage in both samples, but weaker in sample #15μm of 30 % in comparison to 50 % change in #20μm one. In contrast, the relative response of the dark current to vacuum can reach values up to 1000 % at the turn-on voltage. Upon increasing carrier concentration with positive gate voltage, the response tends to the value of illuminated sample, pointing to the electrostatic screening of the molecules on the surface as the reason for lower relative sensitivity under light.

The FET mobility μ can be evaluated by dividing the derivative of the normalized dark current I_{sd}(pA/□) in Fig. 2a,b to the product of the voltage V_{sd} = 1V and capacitance C_i = 1.15×10^{-4} F/m^2 of the 300 nm SiO_2 layer: $\mu = \frac{dI_{sd}(A/□)}{dV_g} \times \frac{1}{V_{sd}C_i}$. The increase in vacuum mobility μ_{HV} relative to that in air μ_{air} is shown in Fig. 2d by the gate voltage dependence of the μ_{HV}/μ_{air} ratio. It can be seen that there is a huge increase in the vacuum mobility, of orders of magnitude at voltages close to turn-on voltage, for both the #15μm and #20μm samples, similarly to the relative change in the dark current ratio $(I_{HV}-I_{air})/I_{air}$ in Fig. 2c. The gate voltage dependences of the FET mobility used to calculate the μ_{HV}/μ_{air} ratio are illustrated by the inset in Fig. 2d for samples #15μm and #20μm in the dark and in air or HV. The curves are shifted towards positive gate voltages when going from vacuum to air, similarly to the dark current curves in Fig. 2a,b, which can be interpreted as an equivalent p-type doping induced by the adsorption of molecules from air.

The mobility increases order of magnitude above turn-on voltage, but the maximum value remains of the order of 10^{-4} cm^2/Vs. Similar very low FET mobility of ~10^{-4} cm^2/Vs has also been

Nanoscale Advances Accepted Manuscript

View Article Online
DOI: 10.1039/D5NA00138B

Open Access Article. Published on 24 February 2025. Downloaded on 2/24/2025 9:59:32 PM.
This article is licensed under a Creative Commons Attribution-NonCommercial 3.0 Unported Licence.

Nanoscale Advances Accepted Manuscript

reported for MoS_2 obtained by sulfurization of pre-deposited evaporated MoO_2 films.[53] The quality of 2D-MoS_2 films obtained by sulfurization of pre-deposited MoO_x thin films was also investigated in Refs. 58,59 by Raman analysis, showing that the residual MoO_3 content in the films decreases by increasing the growth temperature from 700 °C to 800 °C, resulting in a change from strong p-type doping (~10^{13} cm^{-2}) for the growth temperature of 700 °C, to n-type doping ($0.04x10^{13}$ cm^{-2}) for growth at 800 °C. In our FETs with MoS_2 selectively grown at 750 °C by Mo-CVD, a clear intrinsic n-type doping was detected, typically reported for CVD vapor transport layers that have negligible Mo oxide content. Thus, it seems that the Mo-CVD mechanism is closer to that of CVD than to that of local sulfurization of a Mo oxide layer.

As also discussed in Introduction, the high device sensitivity to the molecule adsorption can be explained by the high density of edges and grain boundaries defects as preferential adsorption sites,[32–34] but high defect density strongly affects the field effect characteristics by charge trapping which results in low current and mobility values, depending on device fabrication methods and measurement conditions (contacts resistance, free surface passivation and contact resistance). As shown in our previous publication, the surface resistivity $R(\Omega/\square)$ increases nonlinearly ~24 times when the channel length increases only 4 times (from 5 to 20 μm), the result being explained by the variation of density of the interconnected flakes and their thicknesse.[63] The low conductivity close to the undoped MoS_2 is preferred for higher sensitivity to external stimuli. Therefore, we have chosen in this study to investigate the sensitivity to molecule adsorption on larger channel devices (15 and 20 μm).

View Article Online
DOI: 10.1039/D5NA00138B

Open Access Article. Published on 24 February 2025. Downloaded on 2/24/2025 9:59:32 PM.
This article is licensed under a Creative Commons Attribution-NonCommercial 3.0 Unported Licence.

Nanoscale Advances Accepted Manuscript

The very low mobility of our FETs can be explained by the high density of intrinsic defects, grain boundaries of the interconnected flakes, as well as surface and interface defects, but also by the particular construction of the device. We must add to the explanation of the low current, the fact that the MoS_2 coverage of the FET channel is not 100%, especially for the #20μm sample, as illustrated in Fig. 1c. For our devices, the simplest FET fabrication method was adopted, i.e. the pre-deposited Mo used for the MoS_2 selective growth have been directly bonded for FET electrical measurements just after the MoS_2 growth, without additional metallization photolithographic patterning. In this way, contamination of the MoS_2 surface with the inevitable photoresist residue after the photolithographic process is avoided, which could have influenced the adsorption effect of the molecule studied in this work. In Ref. 51, a protective SiO_2 layer that was selectively etched on the contact areas was used to significantly improve the metal contact with MoS_2 and thus the FET mobility. This procedure is useful for improving a top-gate FET, but not for a bottom-gate FET which must have the MoS_2 surface uncovered for molecule adsorption detection. The aging effect of 2D-MoS_2 by prolonged exposure to air should also be considered in evaluating FET performance. In Ref. 52 it was shown that the MoS_2 FET sensors based on single MoS_2 flakes exfoliated from bulk are more stable after intentional aging for a month, but the electrical mobility was significantly reduced from 1–8 cm^2/Vs to 0.5 cm^2/Vs. In our case the molecule adsorption experiments have been performed after 3 months aging of the MoS_2 samples, and care was taken to obtain reproducible characteristics by repeating the air-vacuum changes and the electric measurements cycles to eliminate intermediary hysteresis states. In same paper Ref. 52, it is shown that by exposure to different solvent vapors the drain current changes in positive (60..300 %) and

View Article Online
DOI: 10.1039/D5NA00138B

Open Access Article. Published on 24 February 2025. Downloaded on 2/24/2025 9:59:32 PM.
This article is licensed under a Creative Commons Attribution-NonCommercial 3.0 Unported Licence.

Nanoscale Advances Accepted Manuscript

negative (-75..-98 %) ranges for polar and non-polar molecules, accompanied by modification in low-frequency noise. Interestingly, we also performed some tests exposing our devices to acetone vapor and found an exponential increase in the source-drain current during exposure toward a saturation value (~ an order of magnitude), as well as unexpectedly large fluctuations in the dc current, which we interpreted as an effect of trapping-detrapping fluctuations of adsorbed polar molecules.

To conclude, our devices exhibit good sensitivity to molecule adsorption, but, for better FET electronic performance, further optimization of the selective MoS_2 growth and device fabrication processes is required.

3.2 Time dependence of the current for light and molecule adsorption excitations

The time-resolved response of I_{sd} to different variations of air pressure and illumination are exemplified in Figs. 3a and 3b for samples #15µm and #20µm, respectively. The experiments shown in Fig. 3 started at atmospheric pressure in dark after devices reached a constant source-drain current.

Device response times for different stimuli (voltage, light, air/vacuum exposure) are between a few seconds and minutes, or even longer in the case of molecule adsorption (Fig. 3). It is mainly an electronic effect of changing the concentration of free carriers by deep-level trapping on surface- and interface-electronic states, or on structural defects in the "bulk" of the 2D MoS_2 few-layers flakes, and by electron transfer or field-induced doping in the case of molecule adsorption and gate voltage variations. In the case of light stimulus, the phenomenon is known as

View Article Online
DOI: 10.1039/D5NA00138B

Open Access Article. Published on 24 February 2025. Downloaded on 2/24/2025 9:59:32 PM.
This article is licensed under a Creative Commons Attribution-NonCommercial 3.0 Unported Licence.

persistent photoconductivity,[68] that has been shown in some cases of ultraviolet light exposure to have a decay-time constant of ~30 days.[69]

In Fig. 3a in period 1 (between zero and 115 min), the sample in air was subject to two on-off illumination cycles. From the initial value (when sample was in dark), I_{sd} current increased by two orders of magnitude in response to turning on the monochromatic light (600 nm wavelength). The current reached 40 – 50 pA and has not saturated within ~ 30 min. The first part of relaxation of the current with time, t, upon turning the light on or off at time t_o can be well represented by a superposition of two exponential decay functions: $A_1 \cdot \exp(-(t-t_o)/\tau_1) + A_2 \cdot \exp(-(t-t_o)/\tau_2)$ where τ_1 and τ_2 are relaxation times, A_1 and A_2 are coefficients (positive or negative for light on and off, respectively). Almost the same relaxation times τ_1 (80 – 85 s) and τ_2 (700 – 800 s) where found for on and off light excitations. A similar response with a slow decrease of current after illumination was observed during the second illumination cycle. After 40 min in dark following the second illumination pulse, the dark current did not relax to initial value from the beginning of the experiment. Pumping of the cryostat with the sample to 4 mbar which started at t= 115 min did not change the current decay, it continued to drop after the last light exposure.

Nanoscale Advances Accepted Manuscript

View Article Online
DOI: 10.1039/D5NA00138B

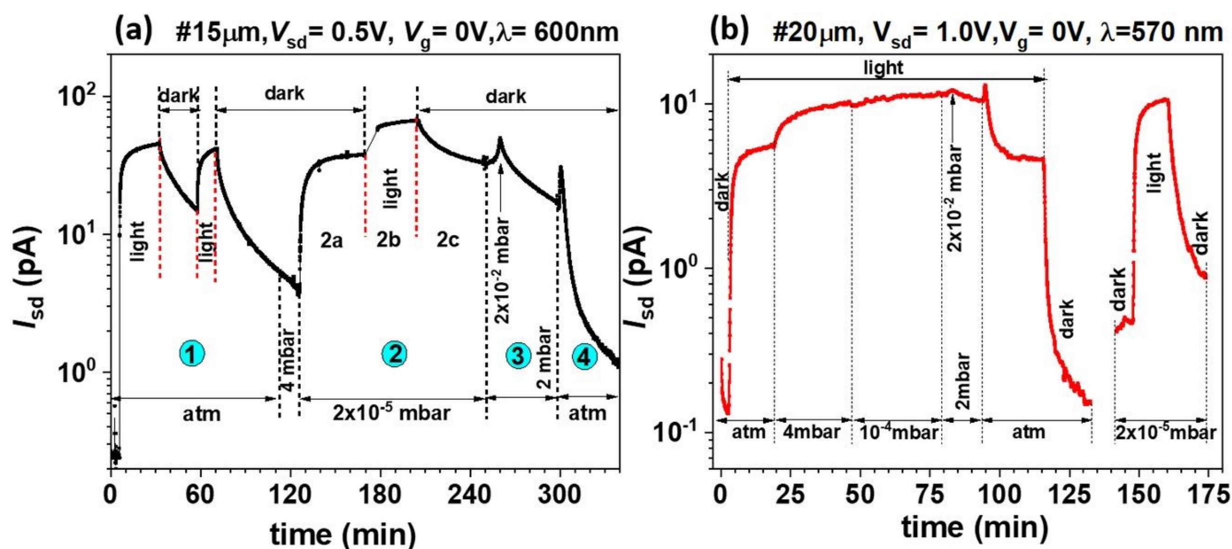

Fig. 3 Time dependence of the source-drain current, I_{sd}, during on-off illumination cycles and vacuum-air pressure variations at room temperature and $V_g = 0$ for samples #15μm (a) and #20μm (b). Labels above the figures contain V_{sd} and V_g voltages during the measurements and light wavelength, λ; air at atmospheric pressure is labeled as "atm"; pressures of 2-4 mbar were obtained by pumping with the fore-vacuum pump and those below 10^{-4} mbar with the turbo-molecular pumps. Different time intervals in figure (a), labeled as 1..4 correlate with constant air pressure times.

The reaction of I_{sd} to the turning on the turbo molecular pump (TMP) to achieve high vacuum (HV) of $2x10^{-5}$ mbar (Fig. 3a, period 2) in dark was relatively fast. The I_{sd} dark current increases in sub-period 2a and reached saturation of ~40 pA at HV. This current increase can be assigned to desorption of molecules, mainly O_2 and H_2O. In high-vacuum, the current further increases to ~76 pA upon illumination (sub-period 2b) and relaxes back to ~40 pA upon switching the light off (sub-period 2c), having almost the same values of the relaxation times τ_1 and τ_2 as those at atm pressure, further suggesting that the photo-carrier recombination is a bulk phenomenon in #15μm sample, less dependent on surface recombination centers induced by the adsorbed molecules.

By switching off the turbo-molecular pump, the pressure increased slowly to 2 mbar maintained by the fore-pump (period 3). During the pressure increase, the dark current I_{sd} first

Open Access Article. Published on 24 February 2025. Downloaded on 2/24/2025 9:59:32 PM.
This article is licensed under a Creative Commons Attribution-NonCommercial 3.0 Unported Licence.

Nanoscale Advances Accepted Manuscript

View Article Online
DOI: 10.1039/D5NA00138B

Open Access Article. Published on 24 February 2025. Downloaded on 2/24/2025 9:59:32 PM.
This article is licensed under a Creative Commons Attribution-NonCommercial 3.0 Unported Licence.

increases sharply, when the pressure reaches the value of 2x10^{-2} mbar to later steadily decreases below the value at the beginning of the period 3. The occurrence of the current peak at 2x10^{-2} mbar was verified by repeating the experiment. The time evolution of I_{sd} during increasing the pressure can be explained by H_2O adsorption, that is able to induce electron accumulation due to its multiple preferential adsorption sites and molecule orientations, as discussed above related to the schematics in Fig. 1a and in Introduction.[31–34] The data can be explained if we assume that initially during the adsorption process, water molecules are electrostatically adsorbed, with the positive pole towards the MoS_2 surface due to H^+ – S^- attractive interaction, inducing accumulation of electrons that generate the current peak at 2x10^{-2} mbar. Over time and by increasing the pressure, the water molecules are adsorbed on the surface of the MoS_2 layer in a more stable position, the one with the depletion effect induced by charge transfer (see the schematics in Fig. 1a). The last period, 4, in Fig. 3a corresponds to a rapid introduction of air at atmospheric pressure. Adsorption of the molecules starts in period 4 by increasing the dark current I_{sd}, which forms a current spike similar to that produced by increasing the pressure to 2x10^{-2} mbar in period 3. The current strongly decreases after that due to the electron-depletion effect of the dominant adsorption mode of H_2O and O_2 molecules.

In Fig. 3b, the monitoring of current I_{sd} of sample #20μm started when monochromatic light (wavelength 570 nm) was turned on with sample in air at atmospheric pressure. As was the case for #15μm sample, the current increased rapidly by over an order of magnitude upon illumination, from I_{sd} of ~0.1 pA to 5.5 pA. The huge photo-response in respect to steady state dark current, also observed in #15μm sample (Fig. 3a, two orders of magnitude increase of I_{sd}), can be

Nanoscale Advances Accepted Manuscript

View Article Online
DOI: 10.1039/D5NA00138B

Open Access Article. Published on 24 February 2025. Downloaded on 2/24/2025 9:59:32 PM.
This article is licensed under a Creative Commons Attribution-NonCommercial 3.0 Unported Licence.

explained by a combination of photo carrier generation and hole trapping that increases the electron concentration to keep local charge neutrality. The relaxation times τ_1 and τ_2 are 50 s and 300 s, respectively; almost a half of the values for sample #15μm.

The light exposure of the sample #20μm is constantly maintained during vacuum experiments in Fig. 3b until $t = 115$ min. The total I_{sd} current increases at 4 mbar by a factor of 2 (I_{sd} = 10 pA). Only a slow, 10%, increase in total current occurs (I_{sd} = 11.7 pA) when vacuum is further increased to 10^{-4} mbar. Also, in contrast to the measurement in dark on sample #15μm (period 3 in Fig. 3a), under light, there is a weaker decrease of the total current by increasing the pressure back to 2 mbar. The I_{sd} current peak at 2x10^{-2} mbar observed very clearly in dark current of sample #15μm, here for sample #20μm under illumination it is much weaker, with the temporary increase of current by 10%. A rapid insertion of air at atmospheric pressure at $t = 93$ min in Fig. 3b, results in a sharp peak of I_{sd} followed by a decrease towards a lower value (I_{sd} = 4.6 pA), close to that measured initially (at t=0) at atmospheric pressure. It is again a similar behavior to the dark current in sample #15μm (period 4 in Fig. 3a). By switching off the light at $t = 115$ min, the dark current in air at atmospheric pressure decreases in ~15 min close to the value of 0.1 pA, the same as at the beginning of the experiment.

In order to evaluate the relaxation times of the light excitation response in sample #20μm in high vacuum, we performed the measurement presented in Fig. 3b starting at $t = 140$ min. The values of the response times τ_1 and τ_2 for sample #20 μm, measured at high vacuum, are 50 s and 280 s for the light on and 35 s and 180 s for light off, respectively. These are shorter than those measured at atmospheric pressure and those found for sample #15μm. This is consistent with the

Nanoscale Advances Accepted Manuscript

View Article Online
DOI: 10.1039/D5NA00138B

Open Access Article. Published on 24 February 2025. Downloaded on 2/24/2025 9:59:32 PM.
This article is licensed under a Creative Commons Attribution-NonCommercial 3.0 Unported Licence.

higher density of thinner flakes that dominate the conduction path in larger electrodes-gap devices and have faster photocarrier recombination.

3.3 Molecule adsorption effects on spectral photocurrent

The spectral dependences of the photocurrent (defined as the difference between the I_{sd} under illumination and the I_{sd}^{dark} in dark before spectral illumination) measured on samples #15 μm and #20μm in vacuum at different pressures and in air at atmospheric pressure are shown in Fig. 4a,b for gate voltage V_g = 0 V. The spectral photocurrent was measured by varying the wavelength from 800 nm to 400 nm in 10 nm steps, 30 s per step, the current acquired at the step end. As shown in Fig. 3, the total current I_{sd} varies on a scale of tens of min, more than two order of magnitude relative to long term dark current, by switching on and off the light. Thus, we can say that the spectral photocurrent presented here with only 30 s per point refers to the faster device response.

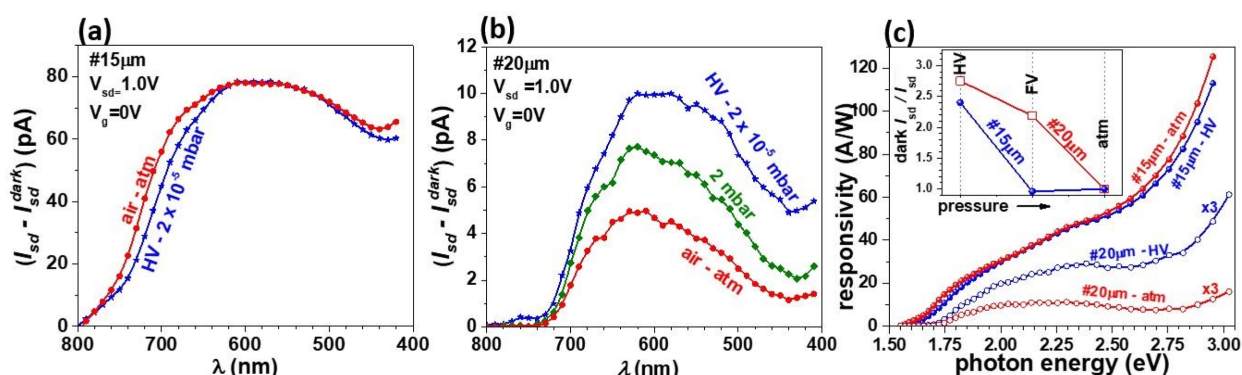

Fig. 4 Spectral photocurrent measured for V_g = 0 on samples #15μm (a) and #20μm (b) at room temperature in vacuum and different pressures; (c) comparison of the spectral photoresponsivity computed based on data of figures (a) and (b) and calibrated spectral illumination power.

In contrast to #15μm (Fig. 4a), in #20μm sample (Fig. 4b), the spectral photocurrent increases with decreasing the air pressure from the atmospheric (atm) to 2–4 mbar (when the

Nanoscale Advances Accepted Manuscript

View Article Online
DOI: 10.1039/D5NA00138B

Open Access Article. Published on 24 February 2025. Downloaded on 2/24/2025 9:59:32 PM.
This article is licensed under a Creative Commons Attribution-NonCommercial 3.0 Unported Licence.

sample is evacuated with the fore-vacuum pump, FVP) and to 2x10^{-5} mbar (evacuated with high-vacuum pump, HV). For better comparison, the spectral responsivity in air, at atm pressure and in HV was computed by normalizing the photocurrent to the spectral illumination power. As can be seen from Fig. 4c, spectral responsivity of sample #15μm is almost independent of the molecule adsorption, the atm and HV curves almost overlap, with a small blue-shift in energy for the measurements in vacuum. In sample #20μm, the photocurrent increases in HV by a factor of 2.1 and is lower than that of the #15μm on the whole spectrum.

The weak photocurrent sensitivity of the sample #15μm photocurrent to the ambient pressure can be explained if we assume that the spectral photocurrent is mainly controlled by photo-excitation and recombination in the "bulk" of the 2D-MoS_2 layer, which is less influenced by the molecules adsorbed on the surface. This is supported by the red shift of the photocurrent threshold from ~1.7 eV in sample #20μm to ~1.6 eV ~ in sample #15μm. Since the bandgap decreases with increasing MoS_2 thickness, the reduced photocurrent threshold in sample #15μm means that the highest photo-conductance path between the contacts leads through thicker interconnected flakes than in sample #20. The dark current of both samples increases by a factor of 2.4 – 2.8 in HV as shown in the inset of the Fig. 4c. It can be seen that sample #15μm is sensitive to gas molecules, but the large number of photogenerated charge carriers screen the effect of molecules on the surface. The increase of dark current in high vacuum and spectral response to the change of ambient pressure in selectively grown 2D-MoS_2 agrees with the reported sensitivity of annealed MoS_2 monolayers to H_2O and O_2 adsorption, observed as a 100-fold increase in light emission efficiency.[30]

Nanoscale Advances Accepted Manuscript

View Article Online
DOI: 10.1039/D5NA00138B

Open Access Article. Published on 24 February 2025. Downloaded on 2/24/2025 9:59:32 PM.
This article is licensed under a Creative Commons Attribution-NonCommercial 3.0 Unported Licence.

In summary, selectively grown 2D-MoS_2 films are sensitive to adsorbed gases and can be potentially used as gas sensors. The samples respond to air-vacuum changes of the total current in full range of λ above the bandgap. As with gate dependence, higher dark conductivity in #15μm means less spectral photocurrent response. Thicker such films are conducting at zero gate voltage (Fig. 2a) and so they can be used as sensors in two-terminal configuration. In both cases, gate voltage and light can be used to tune the responsivity to molecule adsorption.

3.4 Annealing and temperature dependence of the dark current

We saw that source-drain dark current flowing through the devices increased when they were placed in high vacuum, and this was attributed to molecule desorption effect. It is interesting to investigate the high vacuum state of the devices by increasing the temperature, to see if residual adsorbed molecules are further desorbed (supposing that desorption by long time exposure to high vacuum is not completed). The effect of stepwise increase of the temperature to 340 K on samples at high vacuum ($2x10^{-5}$ mbar) is shown in Fig. 5a and 5b for samples #15μm and #20μm, respectively. Each 20 K increase of temperature in Fig. 5a is very fast (21 K/min) and associated with an initial steep increase of current, followed by its slower decrease at constant temperature plateaus (~60 min annealing). Similar behavior is seen in Fig. 5b for #20μm, however the steep increase of the current is less pronounced and appears as delayed decrease of the source-drain current. The current measured at 340 K becomes lower compared with the values measured at 300 K by a factor of 1.8 for #15μm and of 5.5 for #20μm. This decrease at the higher temperature is unexpected in the frame of molecule desorption phenomena previously discussed. If we interpret the annealing results in this scenario of molecule adsorption-desorption phenomena, the initial

Nanoscale Advances Accepted Manuscript

View Article Online
DOI: 10.1039/D5NA00138B

Open Access Article. Published on 24 February 2025. Downloaded on 2/24/2025 9:59:32 PM.
This article is licensed under a Creative Commons Attribution-NonCommercial 3.0 Unported Licence.

current increase in Fig. 5c suggests a desorption of residual molecules followed by their re-adsorption on energetically more favorable sites. The re-adsorption should be accompanied by a stronger electron depletion effect in order to explain the lower current after annealing.

The results obtained by such moderate annealing in high vacuum, with only 40 K temperature increase, might be better explained by redistribution of the trapped electrons. Thus, the fast temperature increase (21 K/min) at each step results in initial current increase due to electron thermally activated from deep traps to conduction band, as in the well-known thermally stimulated current (TSC) phenomenon.[70] After that, at constant temperature, the exited electrons are trapped on deeper energetic levels, including defects on MoS_2 surface and at the interface with SiO_2 layer inducing depletion of free electron concentration in MoS_2 by field effect. In literature, by a stronger annealing at 200–300 ^{o}C, drastically reduced off-current was reported in thick 2D-MoS_2,[71] but, in their case of high temperature annealing in air, the effect was attributed to internal atomic arrangement of MoS_2 atoms, release of a native point defect at the interface, or even to the elimination of photoresist residue included during the fabrication process, similarly to graphene and other 2D-TMD FETs.[64–66]

Nanoscale Advances Accepted Manuscript

View Article Online
DOI: 10.1039/D5NA00138B

Open Access Article. Published on 24 February 2025. Downloaded on 2/24/2025 9:59:32 PM.
This article is licensed under a Creative Commons Attribution-NonCommercial 3.0 Unported Licence.

Nanoscale Advances Accepted Manuscript

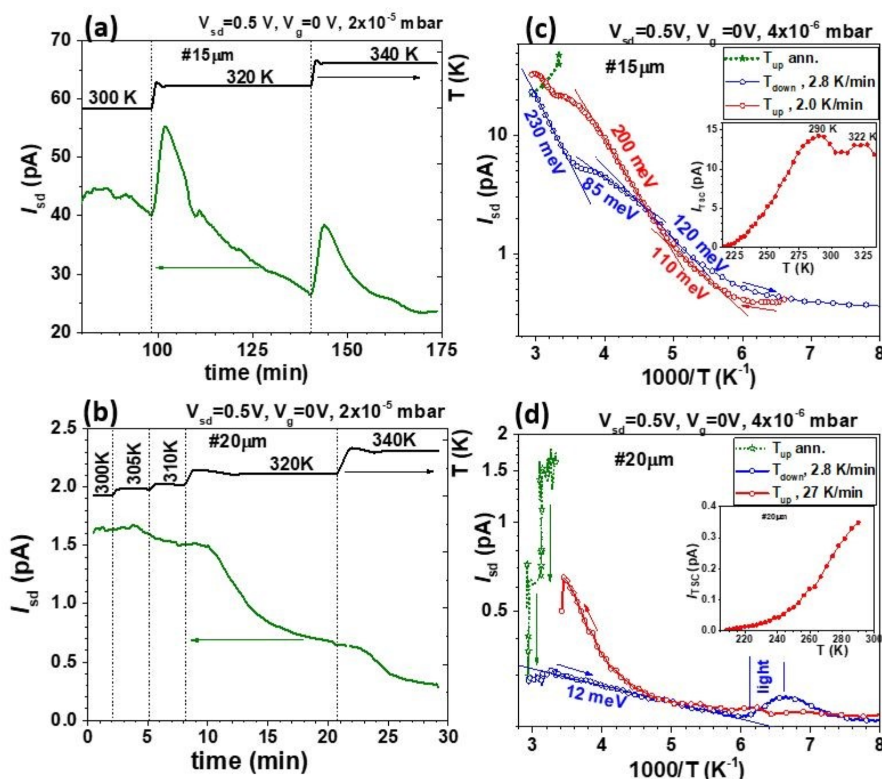

Fig. 5 Temperature dependence of I_{sd} in high vacuum for samples #15μm (a,c) and #20μm (b,d): (a) and (b) I_{sd} time dependence during annealing at higher temperatures than RT (T_{up} ann.); (c) and (d) Arrhenius plot of the I_{sd} temperature dependence for cooling (T_{down}) and heating (T_{up}) at low temperatures. The saturation I_{sd} values at different annealing temperatures (T_{up} ann.) in figures (a) and (b) are also plotted. The insets of (c) and (d) show the corresponding temperature dependence of thermally stimulated current I_{TSC}.

Following the annealing at 340 K in high vacuum, the dark source-drain current in the samples was measured as a function of temperature without breaking the vacuum ($4x10^{-6}$ mbar). The dark I_{sd} measured for both samples by cooling down from 340 K to 100 K and then heating up back to 340 K, are shown Fig. 5c,d. These figures also include the curves T_{up} ann. representing the annealing data in Fig. 5a,b.

The temperature dependence of the current revealed that conducting film in sample #15μm shows extrinsic semiconducting-like behavior. When sample was cooled down with the rate of 2.8 K/min, the current was decreasing with variable rates (curve T_{down} in Fig. 5c) corresponding to different activation energies, which suggests that the sample contains defects with different

View Article Online
DOI: 10.1039/D5NA00138B

Open Access Article. Published on 24 February 2025. Downloaded on 2/24/2025 9:59:32 PM.
This article is licensed under a Creative Commons Attribution-NonCommercial 3.0 Unported Licence.

trapping energies. Thus, in the range of 340–280 K, the activation energy is 230 meV. The current remains almost constant at the plateau down to 260 K to decrease again with activation energies of 85 meV and then 120 meV through a quasi-equilibrium process. This behavior means that the deeper donor state at 230 meV is occupied first during the cool-down and then the shallow levels at 120 meV below the conduction band. Donor states located 250 meV below the conduction band limit attributed to vacant sulfur vacancies are considered in the model proposed in Ref. 45. Using electron paramagnetic resonance (EPR), sulfur vacancies and rhenium impurities were identified as defects in natural MoS_2 crystals, in agreement with Hall measurements that revealed n-type conductivity with a carrier concentration of 2.3×10^{16} cm^{-3} and a mobility of 60 cm^2/Vs at 300 K.[72] Simulating the temperature dependence, they found two activation energies: 89 meV corresponding to shallow donor states with a concentration of 7×10^{15} cm^{-3} attributed to rhenium impurities; another of 241 meV of deeper donor states with a high concentration of 2×10^{19} cm^{-3} related to sulfur vacancies. Based on these literature data, we can attribute the activation energies found in our samples, such as: 230 meV due to sulfur vacancies, while those of 85–120 meV, possibly due to natural impurities, grain boundaries or disorder defects.

At very low temperatures, the current is almost constant at 0.36 pA, a surface or tunneling-like hopping conduction might dominate the electronic transport. In comparison to cooldown (T_{down} in Fig. 5c), the measurement upon warmup at the rate of 2 K/min (T_{up} curve in Fig. 5c) shows almost the same constant current of 0.36 pA for $T < 160$ K, followed by an increase with an activation energy of 110 meV (instead of 120 meV of T_{down} - curve) in the interval 160–210 K. At higher temperatures of 210–300 K, current increased with an activation energy of ~200 meV and

Nanoscale Advances Accepted Manuscript

View Article Online
DOI: 10.1039/D5NA00138B

Open Access Article. Published on 24 February 2025. Downloaded on 2/24/2025 9:59:32 PM.
This article is licensed under a Creative Commons Attribution-NonCommercial 3.0 Unported Licence.

current was higher in T_{up}-curve compared with T_{down}-curve. This hysteresis of $T_{down} – T_{up}$ cycle is due to TSC phenomenon through which, by cooling down, free carriers are trapped at deep levels and then thermally activated when the temperature rises back generating an additional thermally activated current I_{TSC}.[70] This hysteresis is reduced for low trap density and low heating rates. It means that I_{TSC} current (defined as the difference between T_{up} and T_{down} curves, as exemplified by inset of Fig. 5c) is larger when temperature increases faster and shows a peak (or more) at specific temperature (290 °C in this case) depending on trapping energy level and heating rate. The thermally activated current in our case decreased in 270–300 K range, when the current activation energy becomes closer to that of T_{down} curve.

Transport through the #20μm sample upon cooldown (curve T_{down} in Fig. 5d) is almost independent of the temperature (activation energy of 12 meV) and the current is very low, suggesting that there is a very low concentration of free carriers in the film and the dominant current flows via tunneling, e.g. hopping between different states on the surface or in the bulk. Small increase of the current during illumination at 150–160 K verifies that the current flows through the film and induced the filling of deep traps with nonequilibrium electrons. During the fast warmup (with a rate of 27 K/min) electrons are thermally activated from traps and generate the I_{TSC} above 210 K (see inset of Fig. 5d).

The investigations presented in this paper show the complexity of the response of the field-effect device based on interconnected selectively grown 2D-MoS_2 flakes, a multifunctional device very sensitive to changes of various external stimuli (V_g and V_{sd} voltages, light, molecule adsorption, carrier trapping and temperature). High number of defects in film volume and at

Nanoscale Advances Accepted Manuscript

View Article Online
DOI: 10.1039/D5NA00138B

Open Access Article. Published on 24 February 2025. Downloaded on 2/24/2025 9:59:32 PM.
This article is licensed under a Creative Commons Attribution-NonCommercial 3.0 Unported Licence.

surface/interface and grain boundaries have a strong influence on the measurements. The data in Figs 2–5 demonstrate strong and complex dependence of the source-drain current in the devices on the pressure of air and the associated molecules adsorbed on the sample surface. This is consistent with the transport and photoluminescence data of samples prepared by exfoliation or CVD.[30,40] Typically, two types of the air molecules are considered in these reports: O_2 and H_2O. Their effect is most often studied, both theoretically and experimentally, for perfect monolayers. In the monolayer adsorbed O_2 is theoretically predicted to introduce a deep acceptor level in the bandgap.[33] This would mean that O_2 could trap electrons from the conduction band and its desorption in vacuum would lead to higher electron density and conductance. This is consistent with the dark current and photocurrent significantly lower in air than at high vacuum but it doesn't explain the reduction of current upon annealing in vacuum or the current spikes in Fig. 4a and Fig. 5a. While water molecules have been predicted to cause a small increase of the valence band energy at K-point in the monolayer of MoS_2, a very large influence of adsorbed H_2O molecules on carrier recombination and photoluminescence in monolayer was demonstrated.[30] In addition, the devices presented in this study contain regions of thicker layers, which have different band structure. Interactions of polar molecules of water with charge carriers in the presented devices with thicker layers must therefore be also considered. It is possible that when water is first adsorbed, it increases the current (carrier concentration) via its electric dipole orientation (Fig. 4a) to then reorient itself to be neutral (when aligned parallel to the surface) or even reversing the dipole moment, lowering the current in a steady state.

Nanoscale Advances Accepted Manuscript

View Article Online
DOI: 10.1039/D5NA00138B

Open Access Article. Published on 24 February 2025. Downloaded on 2/24/2025 9:59:32 PM.
This article is licensed under a Creative Commons Attribution-NonCommercial 3.0 Unported Licence.

Nanoscale Advances Accepted Manuscript

4. CONCLUSIONS

In conclusion, we investigated the sensitivity of field-effect structures based on 2D-MoS_2 layers selectively grown by Mo-CVD method to molecule adsorption. These devices, fabricated in the bottom-up approach, consist of layers of 2D-MoS_2 interconnected flakes that are selectively grown between pre-deposited Mo source and drain electrodes spaced by 15 µm or 20 µm. The effects of the air pressure, light exposure and gate voltage on current voltage were measured. It was found that both types of samples (#15µm and #20µm) respond similarly to changes of molecular adsorption (mainly H_2O or maybe O_2 from air) by vacuum level variations. In both samples the dark current decreases at atmospheric pressure due to molecule adsorption, which causes electron depletion in MoS_2. Multiple possible adsorption sites and molecule orientation for H_2O relative to MoS_2 surface producing depletion or accumulation can explain the evolution of the current with the air pressure. The response to the light on-off excitation is very high (orders of magnitude), but very slow resulting from a cumulative effect of photo carrier generation and hole trapping that increases the electron concentration by keeping local charge neutrality. For on and off light excitations of #15µm sample, almost the same relaxation times τ_1 (80 – 85 s) and τ_2 (700 – 800 s) were found for HV and atmospheric pressure. Faster response to the light excitation was found in #20µm samples with smaller values τ_1 (35 – 50 s) and τ_2 (180 – 300 s). The dark current was investigated as a function of the temperature after annealing of the samples up to 340 K in HV. The two samples differ significantly in current values and activation energies. The differences between #15µm and #20µm samples can be explained by the higher density of thinner flakes that limit the current in the latter sample. The presented results demonstrate the high sensitivity of the

View Article Online
DOI: 10.1039/D5NA00138B

Open Access Article. Published on 24 February 2025. Downloaded on 2/24/2025 9:59:32 PM.
This article is licensed under a Creative Commons Attribution-NonCommercial 3.0 Unported Licence.

2D-MoS_2 field-effect structures selectively grown by Mo-CVD to the molecule adsorption, as well as possibility to tune the sensitivity by adjusting the growth on patterned substrates with varied gap between electrodes. In both investigated samples, the relative response at RT of the dark current to vacuum can reach values up to 1000 % at the turn-on voltage. The temperature dependence of I_{sd} in high vacuum revealed an activation energy of 230 meV that can be assigned to sulfur vacancies and other shallow levels (85–120 meV), possibly due to natural impurities, grain edges or disorder defects. The result is significant considering simple, inexpensive, bottom-up fabrication technique of the devices that contain non-toxic materials. The demonstration of a large number of structural and boundary defects in selectively grown 2D-MoS_2 interconnected flakes controlling the behavior of studied FET structures could be of great interest for future applications of this versatile device fabrication technique in optoelectrics, or in modern synaptic electronics.

Nanoscale Advances Accepted Manuscript

AUTHOR INFORMATION

Corresponding Author

*Ionel Stavarache − National Institute of Materials Physics, 077125 Magurele, Romania; orcid.org/0000-0002-6405-9912; Email: stavarache@infim.ro.

*Beata E. Kardynal – Peter Grünberg Institute 9 and JARA-FIT, Forschungszentrum Jülich, 52425 Jülich, Germany; Email: b.kardynal@fz-juelich.de.

*Toma Stoica − National Institute of Materials Physics, 077125 Magurele, Romania; orcid.org/0000-0003-2294-8452; Email: toma.stoica@infim.ro.

Author Contributions

View Article Online
DOI: 10.1039/D5NA00138B

Open Access Article. Published on 24 February 2025. Downloaded on 2/24/2025 9:59:32 PM.
This article is licensed under a Creative Commons Attribution-NonCommercial 3.0 Unported Licence.

Nanoscale Advances Accepted Manuscript

The manuscript was written through contributions of all authors. All authors have given approval to the final version of the manuscript.

Conflicts of interest

There are no conflicts to declare.

Data availability

Data will be made available upon request.

ACKNOWLEDGMENT

This work was financially supported by a grant of the Ministry of Research, Innovation and Digitization, CNCS-UEFISCDI, project number PN.111-P2-2.1-PED-2021-2457, as well as by NIMP Core Program Project PC2-PN23080202.

REFERENCES

1. V. Shanmugam, R. A. Mensah, K. Babu, S. Gawusu, A. Chanda, Y. Tu, S. N. Khorasani, M. Försth, G. Sas and O. Das, *Part. Part. Syst. Charact.*, 2022, **39**, 2200031.
2. H. S. Nalwa, *RSC Advances*, 2020, **10**, 30529–30602.
3. Md. M. Uddin, M. H. Kabir, Md. A. Ali, Md. M. Hossain, M. U. Khandaker, S. Mandal, A. Arifutzzaman and D. Jana, *RSC Advances*, 2023, **13**, 33336–33375.
4. D. Gupta, V. Chauhan and R. Kumar, *Inorganic Chemistry Communications*, 2020, **121**, 108200.
5. S. Borghardt, J.-S. Tu, F. Winkler, J. Schubert, W. Zander, K. Leosson and B. E. Kardynał, *Phys. Rev. Mater.* , 2017, **1**, 054001.
6. R. Suzuki, M. Sakano, Y. J. Zhang, R. Akashi, D. Morikawa, A. Harasawa, K. Yaji, K. Kuroda, K. Miyamoto, T. Okuda, K. Ishizaka, R. Arita and Y. Iwasa, *Nature Nanotechnology*, 2014, **9**, 611–617.

View Article Online
DOI: 10.1039/D5NA00138B

Open Access Article. Published on 24 February 2025. Downloaded on 2/24/2025 9:59:32 PM.
This article is licensed under a Creative Commons Attribution-NonCommercial 3.0 Unported Licence.

7. T. Heine, *Accounts of Chemical Research*, 2015, **48**, 65–72.
8. B. Zhu, H. Zeng, J. Dai, Z. Gong and X. Cui, *Proceedings of the National Academy of Sciences*, 2014, **111**, 11606–11611.
9. H. Zeng, J. Dai, W. Yao, D. Xiao and X. Cui, *Nature Nanotechnology*, 2012, **7**, 490–493.
10. D. Mouloua, A. Kotbi, G. Deokar, K. Kaja, M. El Marssi, M. Ali and M. Jouiad, *Materials*, 2021, **14**, 3283.
11. N. Thomas, S. Mathew, K. M. Nair, K. O'Dowd, P. Forouzandeh, A. Goswami, G. McGranaghan and S. C. Pillai, *Materials Today Sustainability*, 2021, **13**, 100073.
12. H. Wang, C. Li, P. Fang, Z. Zhang and J. Z. Zhang, *Chemical Society Reviews*, 2018, **47**, 6101–6127.
13. K. Kalantar-zadeh and J. Z. Ou, *ACS Sensors*, 2015, **1**, 5–16.
14. R. Malik, V. K. Tomer, Y. K. Mishra and L. Lin, *Appl. Phys. Rev.*, 2020, **7**, 021301.
15. Y. Li, Q. Li, Z. Wang, Z. Huang, J. Zhu, A. I. Channa, F. Cui, H. Xu, X. Li, L. Zhou and G. Zou, *Applied Physics Letters*, 2023, **123**, 151103.
16. L. M. Xie, *Nanoscale*, 2015, **7**, 18392–18401.
17. G. Swain, S. Sultana and Kulamani Parida, *Nanoscale*, 2021, **13**, 9908–9944.
18. D. Andrzejewski, M. Marx, A. Grundmann, O. Pfingsten, H. Kalisch, A. Vescan, M. Heuken, T. Kümmell and G. Bacher, *Nanotechnology*, 2018, **29**, 295704.
19. L. Yu, M. Deng, J. L. Zhang, S. Borghardt, B. Kardynal, J. Vučković and T. F. Heinz, *Nano Letters*, 2021, **21**, 2376–2381.
20. D. S. Schneider, A. Grundmann, A. Bablich, V. Passi, S. Kataria, H. Kalisch, M. Heuken, A. Vescan, D. Neumaier and M. C. Lemme, *ACS Photonics*, 2020, **7**, 1388–1395.
21. E. Reato, P. Palacios, B. Uzlu, M. Saeed, A. Grundmann, Z. Wang, D. S. Schneider, Z. Wang, M. Heuken, H. Kalisch, A. Vescan, A. Radenovic, A. Kis, D. Neumaier, R. Negra and M. C. Lemme, *Advanced Materials*, 2022, **34**, 2108469.
22. J. Wu, J. Liu, J. Cui, S. Yao, M. Ihsan-Ul-Haq, N. Mubarak, E. Quattrocchi, F. Ciucci and J.-K. Kim, *Journal of Materials Chemistry A*, 2020, **8**, 2114–2122.
23. T. Stephenson, Z. Li, B. Olsen and D. Mitlin, *Energy Environ. Sci.*, 2014, **7**, 209–231.
24. N. Joseph, P. M. Shafi and A. C. Bose, *Energy & Fuels*, 2020, **34**, 6558–6597.
25. Y. Zhang, Y. Gao, S. Yao, S. Li, H. Asakura, Kentaro Teramura, H. Wang and D. Ma, *ACS*

Nanoscale Advances Accepted Manuscript

View Article Online
DOI: 10.1039/D5NA00138B

Open Access Article. Published on 24 February 2025. Downloaded on 2/24/2025 9:59:32 PM.
This article is licensed under a Creative Commons Attribution-NonCommercial 3.0 Unported Licence.

Catalysis, 2019, **9**, 7967–7975.

26. G. Giuffredi, T. Asset, Y. Liu, P. Atanassov and F. Di Fonzo, *ACS Materials Au*, 2021, **1**, 6–36.
27. X. Wang, L. Meng, B. Li and Y. Gong, *Materials Today*, 2021, **47**, 108–130.
28. P. Luo, F. Zhuge, Q. Zhang, Y. Chen, L. Lv, Y. Huang, H. Li and T. Zhai, *Nanoscale Horizons*, 2019, **4**, 26–51.
29. X. Zhang, Z. Shao, X. Zhang, Y. He and J. Jie, *Advanced Materials*, 2016, **28**, 10409–10442.
30. S. Tongay, J. Zhou, C. Ataca, J. Liu, J. S. Kang, T. S. Matthews, L. You, J. Li, J. C. Grossman and J. Wu, *Nano Letters*, 2013, **13**, 2831–2836.
31. Y. Wang, S. M. Gali, A. Slassi, D. Beljonne and P. Samorì, *Advanced Functional Materials*, 2020, **30**, 2002846.
32. R. Wang, X. Wang, Z. Zuo, S. Ni, J. Dai and D. Wang, *Molecules*, 2022, **27**, 8710.
33. F. Ferreira, A. Carvalho, Í. J. M. Moura, J. Coutinho and R. M. Ribeiro, *Journal of Physics Condensed Matter*, 2017, **30**, 035003.
34. N. S. Bobbitt, J. F. Curry, T. F. Babuska and M. Chandross, *RSC advances*, 2024, **14**, 4717–4729.
35. E. Akbari, K. Jahanbin, A. Afroozeh, P. Yupapin and Z. Buntat, *Physica B: Condensed Matter*, 2018, **545**, 510–518.
36. D.-W. Lee, J. Lee, I. Y. Sohn, B.-Y. Kim, Y. M. Son, H. Bark, J. Jung, M. Choi, T. H. Kim, C. Lee and N.-E. Lee, *Nano Research*, 2015, **8**, 2340–2350.
37. H. Li, Z. Yin, Q. He, H. Li, X. Huang, G. Lu, D. W. H. Fam, A. I. Y. Tok, Q. Zhang and H. Zhang, *Small*, 2011, **8**, 63–67.
38. F. K. Perkins, A. L. Friedman, E. Cobas, P. M. Campbell, G. G. Jernigan and B. T. Jonker, *Nano Lett.*, 2013, **13**, 668–673.
39. A. L. Friedman, F. K. Perkins, E. Cobas, G. G. Jernigan, P. M. Campbell, A. T. Hanbicki and B. T. Jonker, *Solid-State Electronics*, 2014, **101**, 2–7.
40. A. Di Bartolomeo, A. Kumar, O. Durante, A. Sessa, E. Faella, L. Viscardi, K. Intonti, Filippo Giubileo, N. Martucciello, P. Romano, S. Sleziona and M. Schleberger, *Materials Today Nano*, 2023, **24**, 100382.
41. O. Samy, S. Zeng, M. D. Birowosuto and A. El Moutaouakil, *Crystals*, 2021, **11**, 355.
42. B. Radisavljevic, A. Radenovic, J. Brivio, V. Giacometti and A. Kis, *Nature Nanotechnology*,

Nanoscale Advances Accepted Manuscript

View Article Online
DOI: 10.1039/D5NA00138B

Open Access Article. Published on 24 February 2025. Downloaded on 2/24/2025 9:59:32 PM.
This article is licensed under a Creative Commons Attribution-NonCommercial 3.0 Unported Licence.

2011, **6**, 147–150.

43. Z. Cheng, S. He, X. Han, X. Zhang, L. Chen, S. Duan, S. Zhang and M. Xia, *Journal of Materials Chemistry C*, 2024, **12**, 2794–2802.
44. A. Di Bartolomeo, L. Genovese, A. C. Ferrari, L. Iemmo, G. Luongo, T. Foller and Marika Schleberger, *2D Materials*, 2017, **5**, 015014.
45. A. Mamun, Yasuyuki Sainoo, T. Takaoka, A. Ando and Tadahiro Komeda, *RSC Advances*, 2024, **14**, 36517–36526.
46. Y. Guo, X. Wei, J. Shu, B. Liu, J. Yin, C. Guan, Y. Han, S. Gao and Q. Chen, *Appl. Phys. Lett.* , 2015, **106**, 103109.
47. J. Kim, B. Seo, S. Lee, S. Jeong and Y. Roh, *ECS Transactions*, 2017, **77**, 35–39.
48. Salvatore Ethan Panasci, Emanuela Schilirò, G. Greco, M. Cannas, F. M. Gelardi, S. Agnello, F. Roccaforte and Filippo Giannazzo, *ACS applied materials & interfaces*, 2021, **13**, 31248–31259.
49. J. Neilson, M. P. Avery and B. Derby, *ACS Applied Materials & Interfaces*, 2020, **12**, 25125–25134.
50. J. Jiang, Y. Zhang, A. Wang, J. Duan, H. Ji, J. Pang, Y. Sang, X. Feng, H. Liu and L. Han, *ACS Applied Electronic Materials*, 2020, **2**, 2132–2140.
51. P.-Z. Shao, H.-M. Zhao, H.-W. Cao, X.-F. Wang, Y. Pang, Y.-X. Li, N.-Q. Deng, J. Zhang, G.-Y. Zhang, Y. Yang, S. Zhang and T.-L. Ren, *Applied Physics Letters*, 2016, **108**, 203105.
52. R. Samnakay, C. Jiang, S. L. Rumyantsev, M. S. Shur and A. A. Balandin, *Applied Physics Letters*, 2015, **106**, 023115.
53. H. Kim, T. Park, M. Leem, H. Lee, W. Ahn, E. Lee and H. Kim, *Applied Surface Science*, 2021, **535**, 147684.
54. Y. Lee, J. Lee, H. Bark, I.-K. Oh, G. H. Ryu, Z. Lee, H. Kim, J. H. Cho, J.-H. Ahn and C. Lee, *Nanoscale*, 2013, **6**, 2821.
55. K. S. Kim, D. Lee, C. S. Chang, S. Seo, Y. Hu, S. Cha, H. Kim, J. Shin, J.-H. Lee, S. Lee, J. S. Kim, K. H. Kim, J. M. Suh, Y. Meng, B.-I. Park, J.-H. Lee, H.-S. Park, H. S. Kum, M.-H. Jo and G. Y. Yeom, *Nature*, 2023, **614**, 88–94.
56. S. H. Aleithan, T. E. Wickramasinghe, M. Lindquist, S. Khadka and E. Stinaff, *ACS Omega*, 2019, **4**, 9557–9562.
57. M. Chiu, H. Tang, C. Tseng, Y. Han, A. Aljarb, J. Huang, Y. Wan, J. Fu, X. Zhang, W. Chang,

Nanoscale Advances Accepted Manuscript

View Article Online
DOI: 10.1039/D5NA00138B

Open Access Article. Published on 24 February 2025. Downloaded on 2/24/2025 9:59:32 PM.
This article is licensed under a Creative Commons Attribution-NonCommercial 3.0 Unported Licence.

D. A. Muller, T. Takenobu, V. Tung and L. Li, *Advanced Materials*, 2019, **31**, 1900861.

58. S. E. Panasci, E. Schilirò, A. Koos, F. Roccaforte, M. Cannas, S. Agnello, B. Pécz and F. Giannazzo, *Applied Physics Letters*, 2024, **124**, 243101.
59. S. E. Panasci, A. Koos, Emanuela Schilirò, S. D. Franco, G. Greco, P. Fiorenza, F. Roccaforte, S. Agnello, M. Cannas, F. M. Gelardi, Attila Sulyok, M. Nemeth, Béla Pécz and Filippo Giannazzo, *Nanomaterials*, 2022, **12**, 182.
60. K.-Y. Yang, H.-T. Nguyen, Y.-M. Tsao, S. B. Artemkina, V. E. Fedorov, C.-W. Huang and H.-C. Wang, *Scientific Reports*, 2023, **13**, 8378.
61. S. Vangelista, E. Cinquanta, C. Martella, M. Alia, M. Longo, A. Lamperti, R. Mantovan, F. B. Basset, F. Pezzoli and A. Molle, *Nanotechnology*, 2016, **27**, 175703.
62. T. Stoica, M. Stoica, M. Duchamp, A. Tiedemann, S. Mantl, D. Grützmacher, D. Buca and B. E. Kardynał, *Nano Research*, 2016, **9**, 3504–3514.
63. I. Stavarache, C. Palade, A. Slav, I. Dascalescu, A.-M. Lepadatu, L. Trupina, E. Matei, M. L. Ciurea and T. Stoica, *ACS Applied Nano Materials*, 2024, **7**, 5051–5062.
64. Z. Cheng, Q. Zhou, C. Wang, Q. Li, C. Wang and Y. Fang, *Nano Letters*, 2011, **11**, 767–771.
65. J. P. Merino, S. Brosel-Oliu, G. Rius, X. Illa, M. V. Sulleiro, E. D. Corro, E. Masvidal-Codina, A. B. Calia, J. A. Garrido, R. Villa, A. Guimerà-Brunet, M. Prato, A. Criado and E. Prats-Alfonso, *ACS Sustainable Chemistry & Engineering*, 2024, **12**, 9133–9143.
66. J. Liang, K. Xu, Blaec Toncini, B. M. Bersch, B. Jariwala, Y.-C. Lin, J. A. Robinson and S. K. Fullerton-Shirey, *Advanced Materials Interfaces*, 2019, **6**, 1801321.
67. C. Lee, H. Yan, L. E. Brus, T. F. Heinz, J. Hone and S. Ryu, *ACS Nano*, 2010, **4**, 2695–2700.
68. Y.-C. Wu, C.-H. Liu, S.-Y. Chen, F.-Y. Shih, P.-H. Ho, C.-W. Chen, C.-T. Liang and W.-H. Wang, *Scientific Reports*, 2015, **5**, 11472.
69. A. George, M. V. Fistul, M. Gruenewald, D. Kaiser, T. Lehnert, R. Mupparapu, C. Neumann, U. Hübner, M. Schaal, N. Masurkar, L. M. R. Arava, I. Staude, U. Kaiser, T. Fritz and A. Turchanin, *npj 2D Materials and Applications*, 2021, **5**, 15.
70. S. Deb, P. Chakrabarti, H. Chakraborti, K. D. Gupta and S. Dhar, *Applied Physics Letters*, 2019, **115**, 032104.
71. S. D. Namgung, S. Yang, K. Park, A.-J. Cho, H. Kim and J.-Y. Kwon, *Nanoscale Research Letters*, 2015, **10**, 62.

Nanoscale Advances Accepted Manuscript

View Article Online
DOI: 10.1039/D5NA00138B

Open Access Article. Published on 24 February 2025. Downloaded on 2/24/2025 9:59:32 PM.
This article is licensed under a Creative Commons Attribution-NonCommercial 3.0 Unported Licence.

72. F. D. Brandão, G. M. Ribeiro, P. H. Vaz, J. C. González and K. Krambrock, *Journal of Applied Physics*, 2016, **119**, 235701.

Nanoscale Advances Accepted Manuscript

View Article Online
DOI: 10.1039/D5NA00138B

Open Access Article. Published on 24 February 2025. Downloaded on 2/24/2025 9:59:32 PM.
This article is licensed under a Creative Commons Attribution-NonCommercial 3.0 Unported Licence.

Data availability

Data will be made available upon request.

Nanoscale Advances Accepted Manuscript